Journal of Engineering for Gas Turbines and Power. Received September 14, 2023;
Accepted manuscript posted October 04, 2023. doi:10.1115/1.4063632

CONJUGATE MODELLING OF A CLOSED CO-ROTATING COMPRESSOR CAVITY

James Parry, Hui Tang, James A. Scobie, Gary D. Lock, Mauro Carnevale*

**Department of Mechanical Engineering,
University of Bath, Bath, BA2 7AY,
United Kingdom**

ABSTRACT

Robust methods to predict heat transfer are vital to accurately control the blade-tip clearance in compressors and the radial growth of the discs to which these blades are attached. Fundamentally, the flow in the cavity between the co-rotating discs is a conjugate problem: the temperature gradient across this cavity drives large-scale buoyant structures in the core that rotate asynchronously to the discs, which in turn governs the heat transfer and temperature distributions in the discs. The practical engine designer requires expedient computational methods and low-order modelling. A conjugate heat transfer methodology that can be used as a predictive tool is introduced here. Most simulations for rotating cavities only consider the fluid domain in isolation and typically require known disc temperature distributions as the boundary condition for the solution.

This paper presents a novel coupling strategy for the conjugate problem, where unsteady Reynolds Averaged Navier-Stokes (URANS) simulations for the fluid are combined with a series of steady simulations for the solid domain in an iterative approach. This strategy overcomes the limitations due to the difference in thermal inertia between fluid and solid; the method retains the unsteady flow features but allows a prediction of the disc temperature distributions, rather than using them as a boundary condition. This approach has been validated on the fundamental flow configuration of a closed co-rotating cavity. Metal temperatures and heat transfer correlations predicted by the simulation are compared to those measured experimentally for a range of engine-relevant conditions.

Keywords: conjugate heat transfer, computational fluid dynamics, buoyancy-induced flow, rotating cavity

1. INTRODUCTION

Next generation and future aero-engines (*e.g.* Ultra-High Bypass Ratio (UHPR) and open-rotor concepts) will feature High-Pressure (HP) core compressors with smaller dimensions and higher overall pressure ratios. Such engines require compressor blades of reduced span and consequently there is increased sensitivity to tip clearance and associated design margins. The radial distribution of temperature and thermal stress in the discs (to which the blades are attached) governs the radial growth of the rotor and the running clearance between the compressor blades and the outer casing in the mainstream annulus. Reducing the degree of clearance margin associated with an incomplete understanding of disc thermal gradients is an important enabling feature for new technologies. A schematic of an HP compressor with co-rotating discs, shroud, cobs, internal cavity, and central shaft is shown in Figure 1. An axial flow of cooling air passes through the annular gap between the disc cobs and the shaft at low radius, while the shroud of the discs is heated from the hot air in the mainstream annulus.

The combination of the high rotational speed and temperature difference between the bore and shroud results in a buoyancy-induced flow regime in the cavity. The flow is three-dimensional (3D), unsteady and unstable, with a self-organising system that gives great uncertainty to the design process. Such flows create a strongly conjugate problem: the radial distribution of disc temperature influences the flow structure in the rotating cavity, which in turn influences the disc temperatures and radial growth of the discs. In some industrial gas turbines, the clearance between the rotating cobs is minimized and the cavity can become virtually closed. This extreme scenario is a *closed cavity* where no axial flow is ingested nor enthalpy exchanged, and heat transfer is solely by conduction through the hub of the compressor discs. This sealed rotating annulus is a fundamental configuration that lends itself to modelling and computation with reduced complexity.

*Corresponding author: m.carnevale@bath.ac.uk

Journal of Engineering for Gas Turbines and Power. Received September 14, 2023;
Accepted manuscript posted October 04, 2023. doi:10.1115/1.4063632

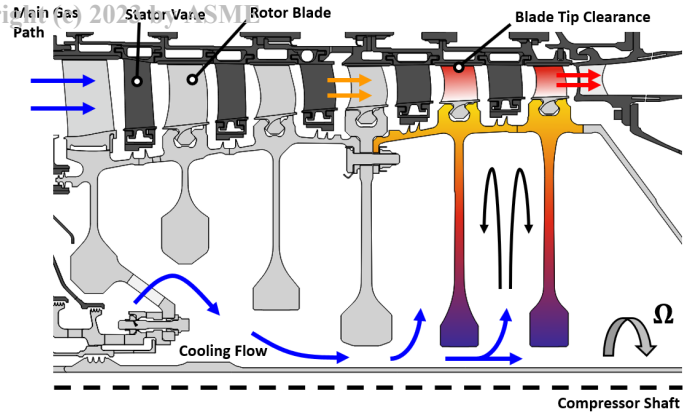

FIGURE 1: CROSS SECTION OF A AERO-ENGINE HIGH-PRESSURE COMPRESSOR, WITH STATIONARY COMPONENTS IN DARK GRAY. ADAPTED FROM JACKSON *ET AL.*[1]

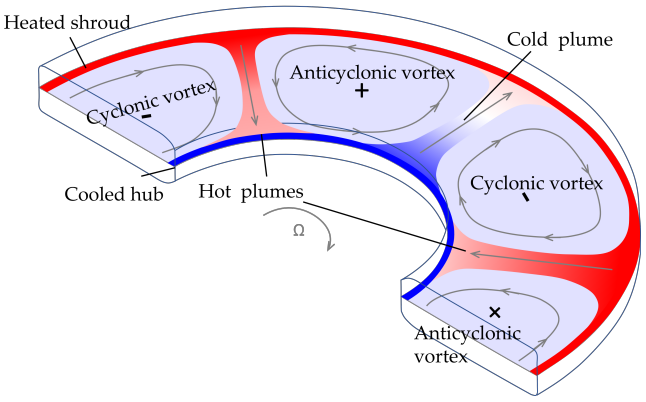

FIGURE 2: BUOYANT FLOW STRUCTURE IN A ROTATING ANNULUS FROM TANG AND OWEN [4]

1.1 Buoyancy-induced Flow Theory

A review of buoyancy-induced flow by Owen and Long [2] discusses the complexity and conjugate aspect of the problem. The physics of the heat transfer is analogous to *Rayleigh-Bénard convection* [3], where gravitational acceleration is replaced by centripetal acceleration $\Omega^2 r >> g$. The fluid will flow radially outward or inward within Ekman layers depending on the relative rotation of the core. Figure 2 shows the unsteady flow structure. Circumferential Coriolis forces are created by the pressure distribution from cyclonic/anticyclonic vortices in the core and shear stresses in the Ekman layers near the discs. Between one pair of vortices, a cold column of air moves radially outward; between the adjacent vortices, a hot column flows radially inwards.

For sealed rotating annuli, the most important nondimensional governing parameters for the fluid are the Grashof (Gr) and rotational Reynolds (Re_ϕ) numbers, and the buoyancy parameter ($\beta\Delta T$):

$$\mathrm{Gr} = \mathrm{Re}_\phi^2 \beta\Delta T \tag{1}$$

$$\mathrm{Re}_\phi = \frac{\rho\Omega r_s^2}{\mu} \tag{2}$$

$$\beta\Delta T = \frac{2(T_s - T_h)}{T_s + T_h} \tag{3}$$

where T_s is the shroud temperature and T_h is the hub temperature. Practical engine design requires fluid-dynamically scaled correlations of heat transfer, usually in the form of power-law exponents. For a known Prandtl number (Pr), the shroud Nusselt number (Nu_s) is usually correlated against the Rayleigh number ($\mathrm{Ra} = \mathrm{Gr}\cdot\mathrm{Pr}$). As a conjugate problem, the properties of the solid domain should also be considered. The Biot number quantifies the ratio of conduction to surface convection in the solid:

$$\mathrm{Bi} = \frac{h_d \delta_d}{k_d} \tag{4}$$

where δ_d is the thickness of the disc at a given location.

Tang and Owen [4, 5] introduced a parameter χ that represents the ratio of kinetic energy in the flow to the heat transfer for the entire system:

$$\chi = \frac{Ma^2}{\beta\Delta T} \tag{5}$$

They derived a model for closed cavities directly relating non-dimensional temperatures for the disc (θ_d) and core (θ_c) to Re_ϕ, $\beta\Delta T$ and χ. The radial distribution of temperature in the core is influenced by χ; above a critical value χ_{crit} the temperature of the fluid core at the shroud is equal to the metal temperature, and the convective heat transfer decreases to zero giving rise to *stratified* flow in the cavity.

1.2 Computational Modelling

Accurate and fast predictive methods are vital for engine clearance design decisions using combined thermo-mechanical models. The unstable phenomena in the fluid present a challenge for Computational Fluid Dynamics (CFD). Successful application of CFD as a design tool requires experimental validation and can be supplemented by physically-based theoretical modelling as documented in Owen *et al.*[6]. The practical application of this research is to improve the predictive capability of industrial conjugate models, including fatigue and component-life applications.

A rotating annulus with cold and hot inner and outer surfaces is the canonical configuration of the rotating compressor cavity, and currently widely used in the literature. Computational studies on this closed cavity configuration lend themselves to simulations using higher fidelity turbulence models. Pitz *et al.* [7] assessed this classic case using large-eddy simulations (LES), observing that the radial velocity in the near-wall region decreased with increasing radius, and capturing unsteady laminar Ekman boundary layers. Recent work by Pitz *et al.* [8] used direct numerical simulations (DNS) on the closed cavity to determine the effect of the Coriolis force on the stability of the fluid core, observing a breakdown of the organised structures when the Coriolis force is removed. Saini and Sandberg [9] performed DNS on the closed-cavity of Bohn *et al.* [10], observing a change in the number of pairs of structure at different Rayleigh numbers. They concluded that using a reduced circumferential domain for computation can affect the formation of these buoyant structures, depending on the Rayleigh number of the flow.

Puttock-Brown *et al.* [11, 12] used unsteady Reynolds-Averaged Navier-Stokes (URANS) simulations with the transitional $k-\omega$ SST model to capture the characteristics of buoyancy-induced flow in an open cavity. They observed enhanced heat

transfer in the near-shroud region for the cold anti-cyclonic vortices and the formation of Rayleigh-Bénard streaks. Saini and Sandberg [13] also observed this phenomenon using Large-Eddy Simulation (LES) of the open-cavity rig of Atkins [14]. Gao and Chew [15] used Wall-Modelled LES to model the open-cavity configuration, using the University of Bath Compressor Cavity Rig for experimental validation [16]. They computed laminar Ekman layers on the discs, with these breaking down near the hub due to the disruptive influence of the axial throughflow.

1.3 Conjugate Modelling

The above computational research considered only the fluid domain, with the disc wall temperature enforced as a boundary condition. This modelling approach neglects the conjugate aspect of the solid-fluid interaction. Fully unsteady 3D models are considered unfeasible as an approach for resolving engine representative simulations due to the slow transient of the solid domains. This leads to unrealistically long computation times.

Initial conjugate models were undertaken by Sun *et al.*[17] and Amirante *et al.*[18], using steady Reynolds-Averaged Navier-Stokes (RANS) simulations and experimental data collected by Atkins [14]. They found a steady fluid domain could not accurately capture the flow physics in the cavity, with the unstable buoyant structures neglected. Tian *et al.*[19] applied URANS to the experiments of Bohn *et al.*[20], indicating the need for a conjugate simulation to capture the effect of throughflow for predicting the temperature of the upstream and downstream discs.

He [21, 22] performed a conjugate simulation coupling the fluid and solid domains using a harmonic-based formulation for interfaces, overcoming the initial transient of the solid domain. The characteristic timescale of the solid was found to be significantly longer than that of the fluid, leading to long convergence times for transient cases. Recent work by Hickling and He [23] assessed the sensitivity of conjugate boundary conditions. LES was used for the fluid domain coupled with a 3D steady-state solid domain. To overcome the long timescale of the solid domain, a frequency-based pseudo-time stepping approach was used. The wall temperature was solved using either the frequency-domain solution for the solid where available, or a one-dimensional (1D) semi-infinite wall transfer function to calculate the low-frequency thermal unsteadiness. Two heating configurations were applied to an open cavity to create the same bulk operating conditions as the experiment of Bohn *et al.*[20]: an axially heated case via the discs and a radially heated case via the shroud. A difference in the formation of fluid structures was observed between the cases, with stronger buoyancy-induced flows in the radially heated configuration. Rayleigh-Bénard streaks were observed in the near-shroud region, as previously computed by Puttock-Brown *et al.*[11, 12].

This paper presents a novel coupling strategy for the conjugate problem, where unsteady simulations for the fluid are combined with a series of steady simulations for the solid domain in an iterative approach. This strategy overcomes the limitations due to the difference in thermal inertia between fluid and solid; the method retains the unsteady flow features but allows a prediction of the disc temperature distributions, rather than using them as a boundary condition. Further, this paper addresses the complex issue of buoyancy-induced flow in compressor cavities by uniquely (in this context) combining experiment, theoretical modelling and conjugate CFD. The experiments provide measurements of shroud heat flux, radial distributions of disc temperature, and unsteady pressure pertaining to the rotating structures. The modelling provides information about the radial distributions of fluid temperature (including the effects of compressibility) and hence shroud heat transfer correlations, and the relationship between radial mass flow and the circumferential distributions of pressure created by rotating structures. The CFD-CHT approach proposed herein is based on a novel in-house multi-fidelity solver, where the solution is time-resolved for the fluid domain and steady for the solid domain. The conjugate simulation calculates the disc temperature distribution independently and is validated using experimental results. The computations provide quantitative insight into the rotating fluid structures, the Ekman layers on the disc, and whether they are laminar or turbulent. As will be demonstrated, this triumvirate of methodology provides consistent and supporting information.

2. METHODOLOGY

2.1 Numerical Solver

All simulations have been conducted using an in-house solver based on the libraries available in the open-source software OpenFOAM-v2006. A new solver was developed based on the conjugate solver *chtMultiRegionFoam*, described by Abbassi *et al.* [24]. This solver uses a cell-centred finite volume scheme in both the solid and fluid domains. The compressible RANS equations are solved in the rotating frame of reference. This strategy was essential to capture expediently the correct development of the boundary layer within an affordable number of elements. Evaluating the gradient of tangential velocity in the absolute reference frame resulted in inaccuracies in the fluid computations within the boundary layer. These limitations were due to machine round-off errors when evaluating the relative change in velocity at high rotational Reynolds number. Without the appropriate development of the Ekman layers, the computational model significantly under-predicted the heat transfer between the fluid and the solid. As observed by Gao *et al.* [25], an incompressible flow model with the Bousinessq approximation poorly captured the heat transfer on the surfaces of a closed cavity at high rotational speeds when compared to a compressible solution. This is due to the way an incompressible model with the Bousinessq approximation calculates density solely using the variation of temperature. For highly rotating flows, the density becomes a function of both the temperature and pressure. Hence, a compressible flow model was selected for the cases presented in this work.

The continuity, momentum and energy equations in the rotating reference frame are given in Equations 6 to 8:

$$\frac{\partial \rho}{\partial t} + \nabla(\rho \vec{\mathbf{V}}_{rel}) = 0 \tag{6}$$

$$\frac{\partial(\rho \vec{\mathbf{V}}_{rel})}{\partial t} + \nabla(\rho \vec{\mathbf{V}}_{rel} \cdot \vec{\mathbf{V}}_{rel}) = -\nabla p + \nabla \cdot \tau + \rho(2\Omega \cdot \vec{\mathbf{V}}_{rel} + \Omega^2 r) \tag{7}$$

$$\begin{aligned} \frac{\partial \rho H}{\partial t} + \nabla(\rho \vec{\mathbf{V}}_{rel} H) + \frac{\partial \rho K_{rel}}{\partial t} + \nabla(\rho \vec{\mathbf{V}}_{rel} K_{rel}) \\ = \frac{\partial p}{\partial t} - \nabla \cdot \mathbf{q} + \rho r \Omega^2 V_r \end{aligned} \tag{8}$$

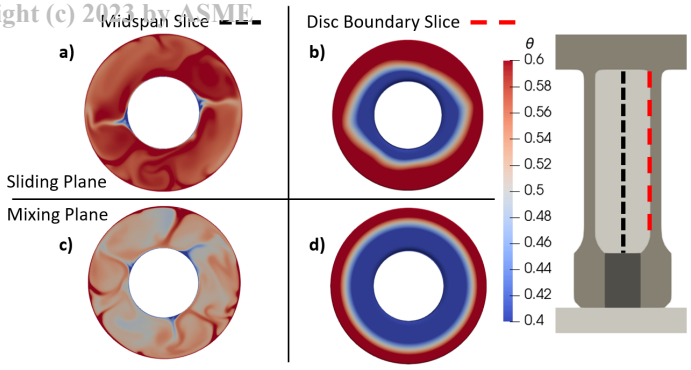

FIGURE 3: INSTANTANEOUS NON-DIMENSIONAL TEMPERATURE CONTOURS OF THE FLUID CORE AND SOLID INTERFACE COMPARING THE SLIDING PLANE AND MIXING PLANE COUPLING

Equation 7 was modified to include the centrifugal and Coriolis forces. Here τ is the viscous stress tensor for the selected turbulence model given in Equation 9,

$$\tau = \mu \left[(\nabla \vec{\mathbf{V}}_{rel} + \nabla \vec{\mathbf{V}}_{rel}^{T}) - \frac{2}{3} \nabla \cdot \vec{\mathbf{V}}_{rel} I \right] \tag{9}$$

where I is the identity tensor. The $k-\omega$ shear stress transport (SST) equation was selected to model the turbulence for all simulations, using the 2003 model by Menter *et al.* [26]. Equation 8 used the relative form of specific kinetic energy $K_{rel} = |\vec{\mathbf{V}}_{rel}|^2/2$. The term $\rho r \Omega^2 V_r$ accounts for the work done by the centrifugal force acting in the relative frame of reference, which was essential to establish the correct distribution of temperature in the rotating fluid core. Using the native OpenFOAM architecture, the fluid domain solves the three conservation equations, while the solid domain solves only the energy equation. The these equations are solved sequentially between each domain until convergence was reached. A second-order least-squares integration scheme was used for resolving the gradients in both regions. An unsteady, implicit, first-order time scheme was used in the fluid. Radiation effects were excluded in the model.

2.2 Conjugate Coupling Strategy

As outlined in the introduction, a significant challenge in conjugate modelling is the difference in timescales of the solid and fluid domains. The unsteady fluid domain is coupled with a steady solid domain, allowing the simulation to progress past the long initial transient in the solid and overcoming the comparatively high thermal inertial of the metal discs to the fluid cavity. The standard implementation for a conjugate interface condition in OpenFOAM is a sliding plane for 3D to 3D coupled domains. This uses mapped fluid and solid patches that fulfil the conservation of energy through equating the temperatures and magnitude of the heat fluxes on both sides of the interface. However, the use of this boundary condition would lead to the high-frequency structures in the fluid domain being transmitted to the solid domain, which are then erroneously used as boundary conditions in subsequent iterations. This unrealistic interaction perturbs the solution and prevents the fluid domain from converging, seen in Figure 3a and 3b where the cold radial plumes in the fluid core are passed to the solid at the coupled boundary.

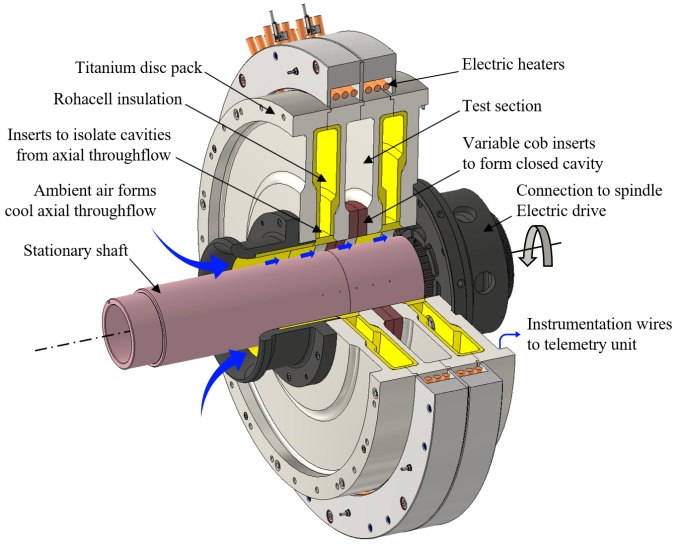

FIGURE 4: UNIVERSITY OF BATH COMPRESSOR CAVITY RIG

To remove these fluctuations, a new boundary condition was implemented that combined the mixing-plane and sliding-plane approaches. By sorting the boundary cells in the fluid domain into radial and axial groups, an average can be made on the temperature of these cells. This process filters out the unsteady temperature fluctuations caused by the buoyant structures, resulting in the distribution seen in Figure 3d. The temperature and heat flux at the patch interface could then be solved using Equations 10 and 11, using the average cell-centre temperature for each radial group in the fluid. This was applied on the fluid-to-solid interface.

$$T_i = \frac{k_f \Delta_f \overline{T_{f,r}} + k_s \Delta_s T_s}{k_f \Delta_f + k_s \Delta_s} \tag{10}$$

$$q = k_f \Delta_f (\overline{T_{f,r}} - T_i) = k_s \Delta_s (T_i - T_s) \tag{11}$$

Due to the axisymmetric nature of the solid, a sliding-plane was used on the reverse solid-to-fluid interface. This approach used a structured, conformal mesh at the coupled boundaries to ensure conservation of flux between the domains.

2.3 Experimental Rig

The University of Bath Compressor Cavity Rig was used to validate the conjugate methodology. The test section of the rig is shown in Figure 4. Four connected titanium discs form three rotating cavities. All measurements for the experiments and computations presented here used a closed central cavity, created by attaching aluminium rings to the cobs at the bore to form a sealed rotating annulus. The adjacent cavities were also sealed from the bore flow using thermally-insulated inserts. The surfaces of the outer cavities and the back surfaces of the co-rotating titanium discs were insulated with Rohacell (a low-conductivity machinable foam) to control the heat transfer through the rig. Radiant heaters were located on the periphery of the shroud of the central discs while an axial throughflow was used to cool the bore of the discs. This created a temperature gradient in the discs, with a maximum $\beta \Delta T = 0.15$. Sixty-four K-type thermocouples were

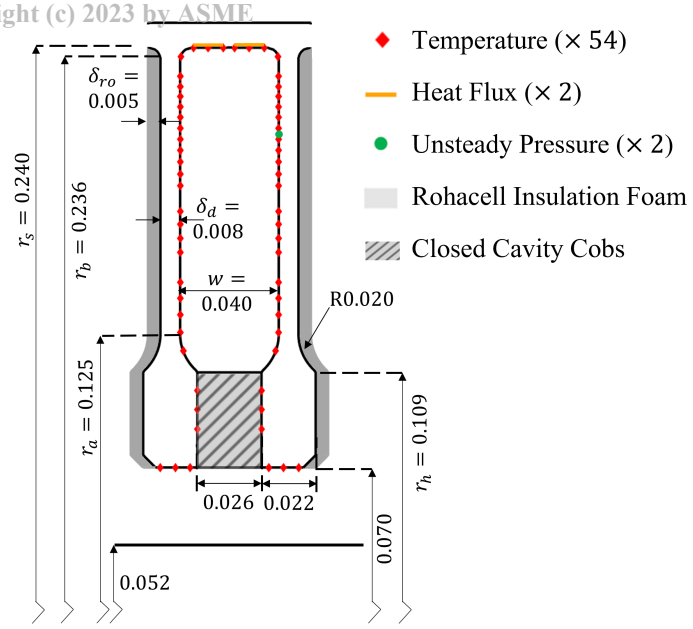

FIGURE 5: CROSS-SECTION OF THE CLOSED CAVITY SHOWING THE INSTRUMENTATION LOCATIONS AND ROHACELL INSULATION (ADAPTED FROM [27]) WITH DIMENSIONS IN M FROM AXIS OF ROTATION

embedded in circumferential grooves to measure the radial distribution of temperature in the upstream and downstream discs of the central cavity, distributed circumferentially in four groups 90° apart. A combined uncertainty is described by a standard deviation of $\pm 0.5°C$ by Jackson *et al.* [16]. An RdF thermopile heat flux gauge was used to measure the heat flux on the shroud of the cavity. Two unsteady pressure sensors (Kulite XCQ-080) located at $r^* = 0.85$ (where $r^* = r/r_s$) and 35° offset were used to record the fluctuations of the buoyant structures. All instrumentation wires were passed through the centre of the spindle to a Datatel telemetry unit. The data from the rotating frame were transmitted to a receiver via an antenna. The fast-response pressure sensors were connected to a separate high-frequency transmitter module; this data was passed through a 1kHz low-pass filter before being sampled at 10kHz to minimize effects of signal aliasing. Thermocouples mounted to rakes on the stationary internal surface of the bore measured the temperature of the axial throughflow. The locations of the instrumentation are presented in Figure 5, with further details of the rig and monitoring equipment reported by Luberti *et al.* [28]. All experimental data used in this study was taken at unsteady-convergence.

2.4 Description of the Conjugate Model

A conjugate model was developed with four coupled domains: Disc Solid, the titanium discs; Cavity Fluid, the fluid in the central cavity; Cob Solid, the aluminium cobs; and Bore Fluid, the axial cooling throughflow. These domains can be identified in Figure 6. Also shown are the boundary conditions, with details in Table 1.

An important aspect of the boundary conditions for the model was setting the magnitude of heat flux through the shroud, *i.e.* the Type I boundary condition. A constant heat flux was imposed to

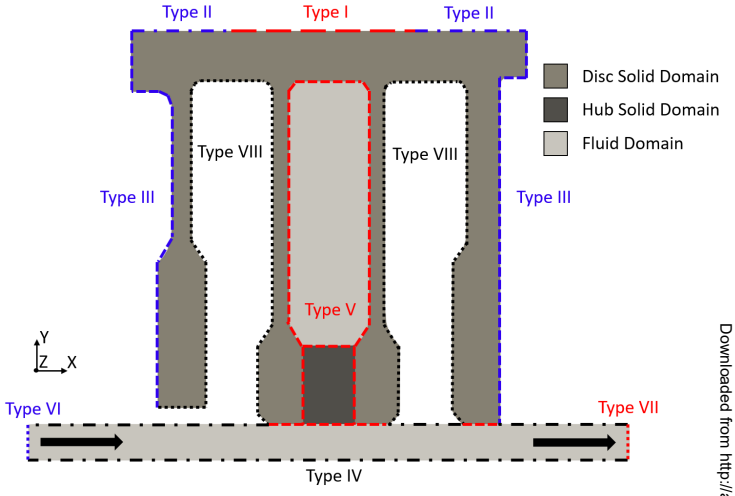

FIGURE 6: CONJUGATE MODEL BOUNDARY CONDITIONS

TABLE 1: BOUNDARY TYPES

Type	Description
Type I	Fixed Heat Flux Shroud
Type II	Free-rotating Cylinder Convection
Type III	Free-rotating Disc Convection
Type IV	Adiabatic
Type V	Domain Interfaces
Type VI	Bore Inlet
Type VII	Bore Outlet
Type VIII	Adjacent Cavity Convection

match the buoyancy parameter $\beta\Delta T$ and a constant rotation speed for the rotational Reynolds number Re_ϕ were matched with the appropriate experimental cases.

The outer surfaces of the shroud and discs were exposed to atmospheric temperatures, hence two convective boundary conditions (Type II and Type III) were applied. A forced convective heat transfer correlation for a free-rotating cylinder surface was used for the Type II boundaries. Here a fixed ambient temperature T_{amb} and heat transfer coefficient h_{cyl} were used, calculated using Equation 12.

$$h_{cyl} = \frac{Nu_{cyl} k_d}{r_{so}} \tag{12}$$

A forced convective heat transfer Nusselt correlation for a free-rotating-disc surface by Owen and Rogers [29] was applied to the Type III boundaries considering a fixed ambient temperature T_{amb}. A constant heat transfer coefficient h_{so} was applied, evaluated using Equation 13:

$$h_{so} = \frac{Nu_{so} k_d}{r_{so}} \tag{13}$$

The 5 mm layer of Rohacell insulation shown in Figure 4 that lines the outer cavities does not completely insulate the discs, with non-

TABLE 2: SOLID DOMAIN THERMAL PROPERTIES

Property	Disc Solid	Cob Solid
Material	Titanium Ti-6Al-4V	Aluminium Al-6082
ρ (kg/m^3)	4620	2700
k (W/mK)	7	180
c_p (J/kgK)	565	890

TABLE 3: DOMAIN ELEMENT COUNT FOR SELECTED MESH

Region	No. of Elements (10^6)	Resource Proportion
Disc Solid	1.45	13.8%
Cob Solid	0.14	1.4%
Cavity Fluid	1.77	50.3%
Bore Fluid	1.21	34.5%

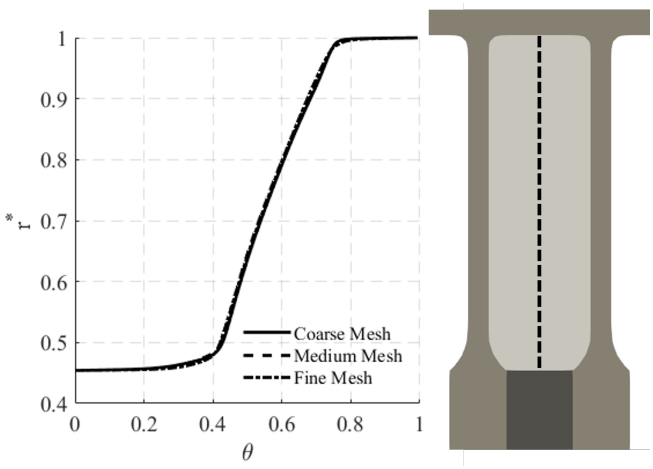

FIGURE 7: VARIATION OF CAVITY CORE TEMPERATURE WITH RADIUS FOR THREE DIFFERENT FLUID-ONLY MESHES

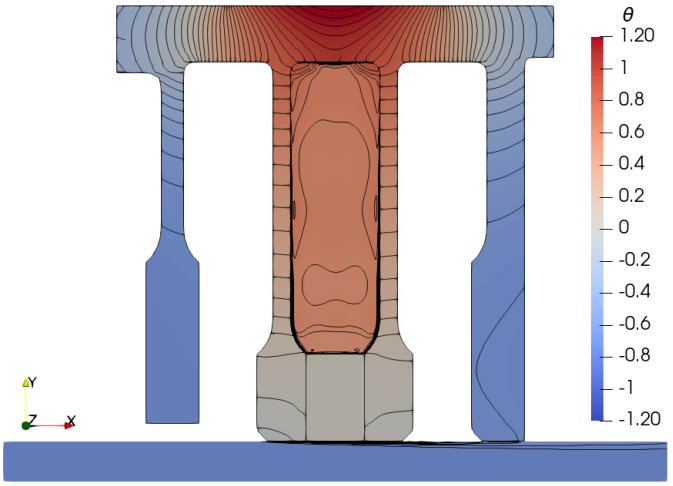

FIGURE 8: INSTANTANEOUS TEMPERATURE CONTOUR FOR THE FULL CONJUGATE MODEL FOR CASE 2

negligible heat transfer between these cavities and central discs. Assuming heat transfer via conductive laminar Ekman layers (see Tang and Owen [4]), the Type VIII boundary condition was used to approximate this heat transfer to a free convection boundary. An ambient adjacent cavity temperature was derived using core temperature correlations by Nicholas *et al.*[27] and a cumulative heat transfer coefficient given by h'_{d-adj} in Equation 14:

$$h'_{d-adj} = \left(\frac{1}{h_{d-Ek}} + \frac{\delta_{ro}}{k_{ro}}\right)^{-1} \tag{14}$$

This equation is a combination of the heat transfer through the Rohacell, where k_{ro} is the thermal resistivity of Rohacell and δ_{ro} is the thickness of Rohacell lining the cavity, and h_{d-Ek} is the average disc heat transfer coefficient for a laminar Ekman layer, given by Equation 15:

$$h_{d-Ek} = \frac{\delta^*_{Ek}}{k_f} \tag{15}$$

Here δ^*_{Ek} is the effective Ekman layer thickness given by Equation 16:

$$\delta^*_{Ek} = \pi\delta_{Ek} = \pi\sqrt{\frac{\mu}{(\rho\Omega)}} \tag{16}$$

A conformal, multi-block structured mesh was used, with an O-grid applied to the cavity fluid domain. The thermophysical properties of the solid domain are taken from Luberti *et al.*[28] and summarised in Table 2.

A mesh independence study was performed on the central rotating cavity domain, as was the most sensitive region of the model where the most complex fluid phenomena occur. A 360° model was used to ensure the proper development of the unsteady structures. Three fluid-only meshes were compared at the maximum rotational Reynolds number and buoyancy parameter, $\mathrm{Re}_\phi = 2.94 \times 10^7$ and $\beta\Delta T = 0.13$. Experimental wall temperatures collected by Jackson *et al.*[16] were enforced on the cavity boundaries. A coarse mesh was made with 1.1M cells, a medium mesh with 1.8M cells, and a fine mesh with 2.5M cells. Figure 7 shows the radial distribution of non-dimensional circumferential and time-average core temperature in the axial mid-plane. This is defined using Equation 17:

$$\theta = \frac{T - T_h}{T_s - T_h} \tag{17}$$

Here, T_s and T_h are the experimental hub and shroud temperatures. The simulations were run till an unsteady convergence was reached to remove the initial transient, with a further 180 revolutions to acquire time-averaged data in the fluid.

A Richardson extrapolation was performed on the core temperature of the three meshes and the Grid Convergence Index (GCI) was evaluated for each refinement:

$$GCI = \frac{F_S|\varepsilon|g_r^2}{(g_r^2 - 1)} \tag{18}$$

where g_r is the grid refinement, ε is the relative error evaluated

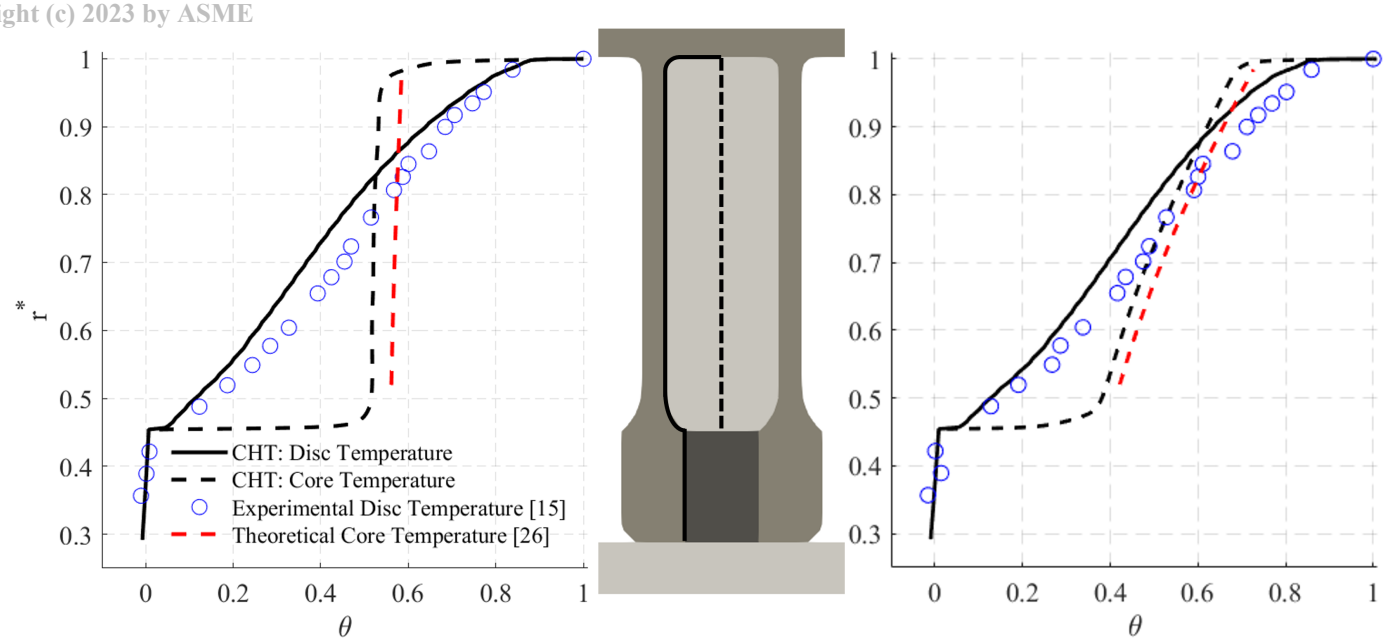

FIGURE 9: VARIATION OF DISC AND CORE TEMPERATURE WITH RADIUS FOR: A) CASE 2 B) CASE 4

using the prediction of the finest level, and $F_S = 1.25$ is a safety factor as suggested by Roache [30]. The GCI has been evaluated for the refinement between the coarse to medium meshes and between medium to fine meshes, respectively as $GCI_{med} = 0.23$ and $GCI_{fine} = 0.34$. As the condition $GCI_{fine} \approx g_r^2 GCI_{med}$ is satisfied, the solution has been demonstrated to be grid independent and the medium mesh refinement was selected for all other simulations presented in this paper. A full breakdown of the number of elements in each region can found in Table 3. The wall-normal spacing in the fluid domains of 0.08 mm is $\approx 0.2\delta_{Ek}$ at maximum Re_ϕ, giving an average $y^+ = 0.69$. 360 time steps were used per disc revolution, giving a maximum Courant number of 0.37 in the cavity fluid and 0.85 in the bore fluid.

2.5 Plume Model

As discussed in the Introduction, the theoretical models developed by Tang and Owen [4] show the influence of Re_ϕ, $\beta\Delta T$ and χ on the non-dimensional temperatures, θ_d and θ_c. Lock *et al.*[31] presented correlations for shroud Grashof number and heat transfer using the definitions, given in Equations 19 and 20:

$$Gr_s = \frac{\Omega^2 r_s (w/2)^3 \beta (T_s - T_{c,b})}{\nu_{c,b}^2} \tag{19}$$

$$Nu_s = \frac{q_s (w/2)}{k_{c,b}(T_s - T_{c,b})} \tag{20}$$

where, $T_{c,b}$ and $k_{c,b}$ are the core temperature and thermal conductivity of air at the outer radius of the uniform section of the diaphragm, r_b.

In the model, the radial plumes act as the mechanism of transferring heat from the hot shroud to the cold hub. The mass flow rate of the radial plumes is linked to the pressure difference between the vortex pairs, using an average Δp to calculate the pressure coefficient C_p, given in Equation 21. Lock *et al.*[31] identified a correlation between the plume mass flow rate C_w and shroud Grashof number Gr_s:

$$C_w = \frac{\dot{m}}{\mu w} = \frac{n Re_\phi C_p}{2} \tag{21}$$

$$C_p = \frac{\Delta p}{\rho \Omega^2 r_s^2} \tag{22}$$

For the disc heat transfer, the model assumes conductive Ekman layers on the disc surfaces. The calculated heat flux is a function of the rotational Reynolds number and the temperature difference between the disc and core. The core temperature was shown to be influenced by compressibility, which can be quantified by the compressibility parameter χ. A detailed derivation can be found in Tang and Owen [4], with all symbols defined in the nomenclature.

3. RESULTS

The results presented in this section compare three different disciplines of analysis: *experimental data* collected by Jackson *et al.*[16] presented in blue; *theoretically-predicted* values using theoretical models by Tang and Owen [4] presented in red; and the conjugate computational results presented in black. The five operating conditions shown in Table 4 were considered over a wide range of rotational Reynolds numbers ($0.79 < \mathrm{Re}_\phi < 3.04\times10^7$), buoyancy parameter ($0.06 < \beta\Delta T < 0.14$) and compressibility parameter ($0.13 < \chi < 5.34$). Also listed in the Table are the non-dimensional heat fluxes used for the Type I boundary defined using Equation 23 and the adjacent cavity core temperatures for the Type VIII boundary for each case.

$$\xi = \frac{2 r_s^2 q}{k_d t_d (T_s - T_h)} \tag{23}$$

TABLE 4: NON-DIMENSIONAL PARAMETERS

Case	1	2	3	4	5
$\mathbf{Re}_\phi$ (10^6)	0.80	0.79	3.04	2.96	3.04
$\beta\Delta T$	0.07	0.14	0.10	0.13	0.06
ξ_{so}	236	252	360	340	290
θ_{c-adj}	-0.16	-0.30	0.04	-0.33	0.33
χ	0.28	0.13	2.92	2.19	5.34
$\mathbf{Gr}_s$ (10^7)	0.81	1.20	10.28	13.46	6.57
$\mathbf{Nu}_s$	9.2	12.1	23.3	29.0	9.2
C_w (10^4)	1.76	3.08	5.90	7.98	0.20
$\mathbf{Bi}_s$	0.04	0.06	0.12	0.15	0.05

All simulations were run to convergence with data collected over a subsequent 200 disc revolutions. A typical solution was obtained in 20k core-hours over three days on 288 cores on Intel Xeon (Broadwell) processors. To evaluate the efficiency of the method, a comparison against the fluid-only simulation from the mesh independence study was performed. The fluid simulation required 6.8k core hours to complete 200 disc revolutions, with the conjugate simulation requiring 10k core hours, roughly 1.5× longer. However, twice the number of loop operations were solved in this time when considering the added disc, cob and bore domains. As shown in Table 3, 85% of the computation time is dedicated to the fluid parts of the model.

3.1 Conjugate Thermal Modelling

Figure 8 shows the non-dimensional temperature for the full model for Case 2, where θ is given using Equation 17. As expected, the aluminium is almost isothermal. All temperatures presented hereafter are in non-dimensional form. These are both time- and circumferentially-averaged.

The computed temperatures are presented in Figure 9, alongside steady-state experimental data and theoretical core temperatures from Jackson *et al.*[16] and Nicholas *et al.*[27]. Cases 2 and 4 compare constant $\beta\Delta T$ at low and high Re_ϕ respectively, but the conjugate model successfully captured the radial distribution and gradient of both disc and core temperature for the four experimental cases (Cases 1-4). The conjugate computations show good quantitative agreement with the experiments and show the gradient in disc temperature is insensitive to $\beta\Delta T$ and Re_ϕ, consistent with Jackson *et al.*[16].

The computed core temperatures are also shown in Figure 9, capturing the main characteristics predicted by the theory. Note the theory only produces results across the uniform section of the diaphragm ($0.52 < r^* < 0.96$). The core temperature is influenced by the shroud and disc heat transfer and increases with radius due to the effects of compressibility at large Re_ϕ. Case 2 features a low χ with small effects of compressibility, with little variation of θ_c with radius. In contrast, Case 4 features large χ and compressibility has a strong influence in the core, *i.e.* a

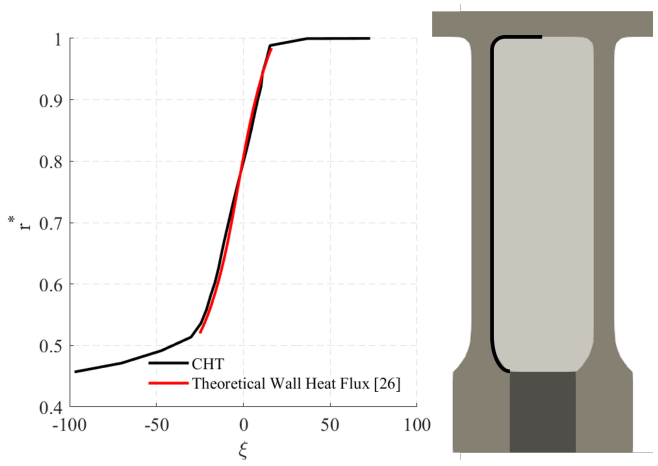

FIGURE 10: VARIATION OF WALL HEAT FLUX WITH RADIUS FOR CASE 2

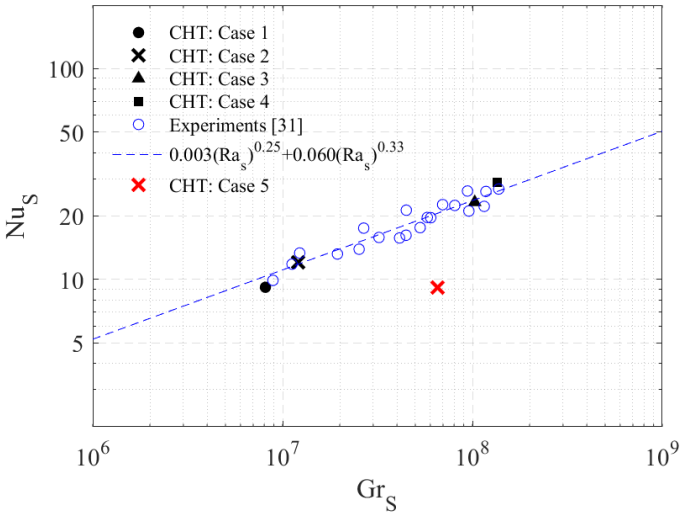

FIGURE 11: SHROUD HEAT TRANSFER CORRELATION FOR CLOSED CAVITY

greater rise of θ_c with radius. The computations indicate thin regions (or boundary layers) where there are marked gradients in temperature near the shroud and hub ($r^* < 0.52$ and $0.96 < r^*$). A crossover of the disc and core temperatures can be seen at $r^* \approx 0.85$ for all cases. This is linked to an inflexion in the disc temperature gradient and corresponds to a change in the wall heat flux.

Figure 10 shows the radial variation of computed non-dimensional wall heat flux given using Equation 23. Theoretical correlations from Nicholas *et al.*[27] are presented for comparison. Near the shroud of the cavity, a positive heat flux shows the discs transferring heat to the cavity. The direction of heat flux reverses for $r^* < 0.8$ where the cavity temperature becomes greater than that of the discs. Capturing the correct conjugate physics in both the solid and the fluid underpins the computations of the correct temperature gradient that drives the buoyancy-induced regime discussed in section 3.2. Though not shown here, Cases 1 and 3 returned similarly good agreement between computation,

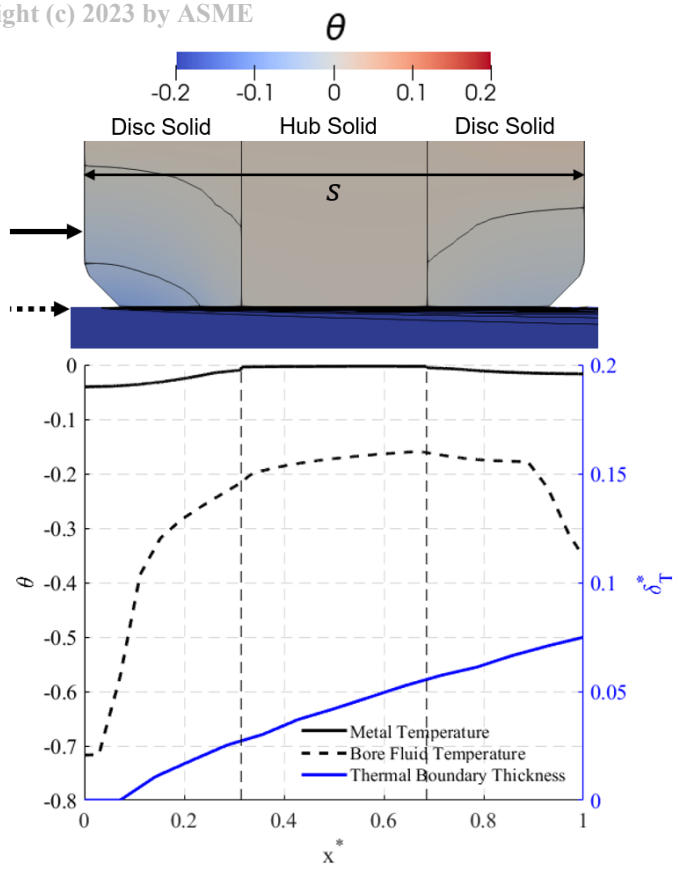

FIGURE 12: AXIAL DISTRIBUTION OF SOLID AND FLUID TEMPERATURES WITH BORE FLOW THERMAL BOUNDARY GROWTH FOR CASE 2

experiment and theory. Table 4 shows the Biot number at the disc shroud using Equation 4. With Bi << 1 we can see the convection of the surface is much greater than the conduction resistance in the solid, with a small gradient of temperature through the shroud.

Figure 11 shows the variation of computed shroud Nusselt number (Nu_s) with shroud Grashof number (Gr_s) for the five cases shown in Table 4. The experimental measurements and correlation from Pernak *et al.*[32] are shown for comparison. Nu_s and Gr_s have been defined in Equations 19 and 20, where the temperature $T_{c,b}$ was evaluated at $r^* = 0.96$. This location was chosen to ensure the reference temperature was in the core outside the shroud boundary layer. Cases 1-4 match closely with the experimental correlation. It is important to note all experimental data were taken from cases where $\chi < 2.92$, where the buoyancy effects were sufficiently high that coherent rotating structures in the closed cavity were measured. Case 5 features $\chi = 5.34$ and does not follow the correlation; as discussed in Section 3.3, at this condition the core temperature at high radius approaches the temperature of the shroud and the flow is in transition to stratification, with $\xi \rightarrow 0$ at the shroud.

Figure 12 compares the metal temperature in the hub with the temperature in the viscous sub-layer of the fluid in the axial throughflow for an instantaneous solution for Case 2. The distance $x^* = x/s$ is the non-dimensional width of the hub, and the thermal boundary layer $\delta_T^* = \delta_T/D$ is non-dimensionalised with the width of the bore annulus (D). The thermal boundary layer for the axial throughflow starts growing at the solid-fluid interface as adiabatic conditions are applied for $x^* < 0.07$, with adiabatic inserts present upstream of the hub. The trends for the fluid and solid temperatures illustrate a decreased cooling effectiveness with axial distance corresponding to an increase in δ_T^*. The importance of a conjugate model is highlighted here, with the non-symmetry caused by the flow physics and not a boundary condition. The ability to capture both the axial and radial distributions of disc temperature makes this conjugate tool suitable for prediction, without the requirement of known disc temperatures as boundary conditions for the model.

3.2 Flow Structure

Instantaneous plots of pressure and radial velocity from the axial mid-plane of the fluid cavity for cases 2 and 4 are shown in Figure 13. Pressure has been normalised using Equation 24 and radial velocity has been made non-dimensional with respect to the relative disc speed $\Omega_d r$.

$$\hat{C_p} = \frac{p - \bar{p}}{0.5\rho\Omega_d^2 r_s^2} \tag{24}$$

The contour of $\hat{C_p}$ illustrates the circulating structure, with the regions of relative negative pressure (marked −) corresponding to the hot anti-cyclonic vortices and the positive regions (marked +) to the cold cyclonic vortices. Cases 2 and 4 feature three and four vortex pairs respectively. This is consistent with the experiments [16], noting that for a fixed closed-cavity geometry the number of vortex pairs depends on Re_ϕ. Radial plumes are observed adjacent to these vortices, with cold outflow and warm inflow.

Jackson *et al.*[16] determined the speed of the vortex pairs, Ω_s, relative to the disc rotation, Ω_d using the cross-correlation of signals from unsteady pressure sensors. Using the same methodology, the ratio of structure speed to disc speed, Ω_s/Ω_d, was computed as a function of radius in Figure 14, along with the time- and circumferentially-averaged tangential speed of the core Ω_c. Shown for Case 2, the structures are in near solid-body rotation with the disc and in good agreement with the experiment. The magnitude of the slip is broadly uniform (< 0.7%), with a slight increase with radius. The average core and structure speeds differ. In the near-shroud region $\Omega_c > \Omega_d$ with a reversal near the hub, ensuring conservation of angular momentum in the cavity. This radial asymmetry can be attributed to the interactions of the buoyant plumes with the core. Hot plumes carry flow radially inward with reduced momentum; while cold plumes carry the flow radially outward with greater momentum, as shown in Figure 13 b and d.

As discussed in Section 2.5, Lock *et al.*[31] identified a correlation between the non-dimensional plume mass flow rate C_w and shroud Grashof number Gr_s - see Equation 19. The computations numerically integrated the radial mass flow rate with results shown in Figure 15. Also shown are the experimental data and correlation from Pernak *et al.*[32]. All four buoyant-flow cases (Cases 1-4) show good agreement with the experimental

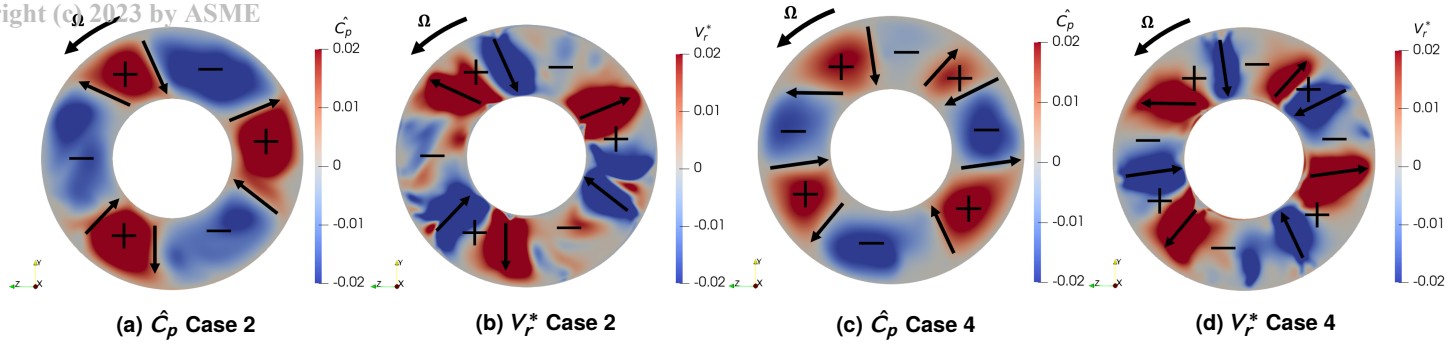

(a) $\hat{C}_p$ Case 2 (b) V_r^* Case 2 (c) $\hat{C}_p$ Case 4 (d) V_r^* Case 4

FIGURE 13: INSTANTANEOUS MID-PLANE SNAPSHOTS OF NORMALISED PRESSURE AND RADIAL VELOCITY FOR CASE 2 AND 4

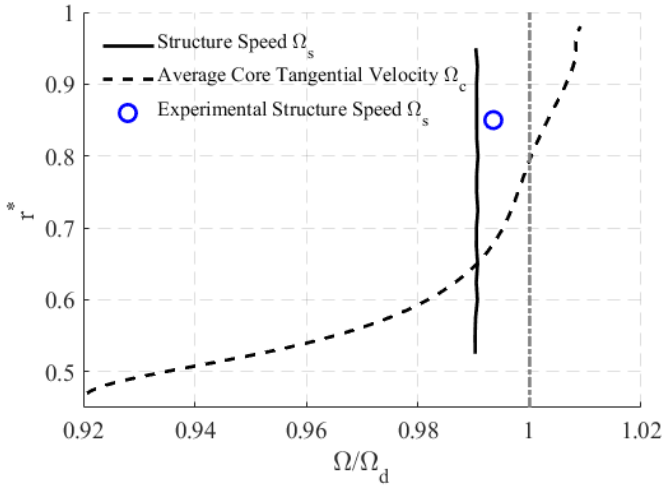

FIGURE 14: STRUCTURE SPEED AND CORE TANGENTIAL VELOCITY RELATIVE TO DISC SPEED FOR CASE 2

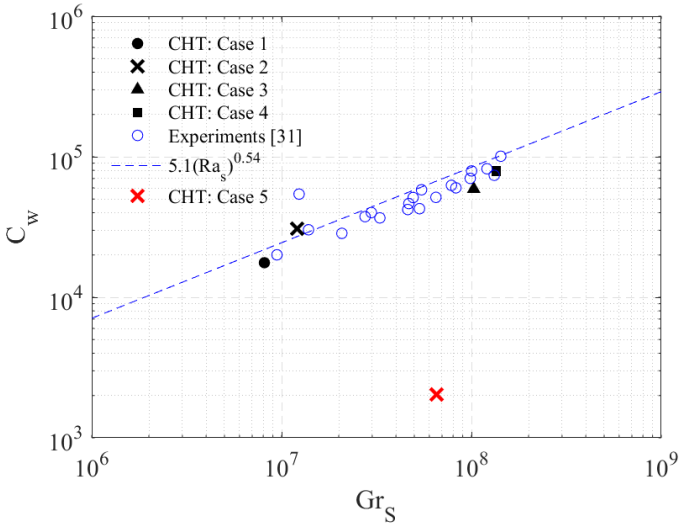

FIGURE 15: VARIATION OF NON-DIMENSIONAL PLUME MASS FLOW RATE WITH SHROUD GRASHOF NUMBER

data, with C_w increasing as Re_ϕ and $\beta\Delta T$ increase as the buoyancy forces become more dominant. Experimental data was only available when the pressure variation from the flow structures was measured. Lock *et al.*showed that $C_p \rightarrow 0$ at high χ. In a similar argument to that discussed with reference to Figure 11, Case 5 ($\chi = 5.34$) does not follow the correlation. This is discussed further in Section 3.3.

Figure 16 shows the time- and circumferentially-averaged radial velocities in the near-wall region for the upstream disc at different radial locations for Case 2. The velocity V_r^* is normalised by the relative disc speed Ωr. The non-dimensional wall distance Δw^* is the ratio of the dimensional distance Δw and the thickness of the laminar Ekman layer δ_{Ek}. For all cases, the average radial velocity reduces to zero in the core at the edge of the boundary layer. Near the hub, a strong positive radial velocity is observed in the Ekman layer. The peak value diminished with increasing radius and reverses near the shroud. This is consistent with the radial distribution of circumferentially averaged core speed, with $\Omega_c/\Omega_d < 1$ near the hub and > 1 near the shroud. This is consistent with the observations of Gao and Chew [33] when assessing the closed cavity configuration of Bohn *et al.*[10].

Figure 17 shows instantaneous non-dimensional heat flux ξ on the annular surfaces of the shroud and hub for Case 2. These contours are juxtaposed with those of normalised pressure in the mid-span of the fluid. Regions of enhanced heat transfer on the hot shroud are observed adjacent to the cold cyclonic vortices. The cold fluid in the flow mixes with the hot fluid in the shroud boundary layer in these regions. This effect is also seen on the hub, with a similar effect occurring with the hot anti-cyclonic vortices.

3.3 Effect of High-χ

Stratified flow occurs when the temperature gradient is insufficient to form buoyant structures, and shroud heat transfer is dominated by conduction, not convection. Typically stratification is a complex process, with portions of the cavity influenced by disc heat transfer. Stratification in a steady-state case was demonstrated by Lock *et al.*[31] and in a transient case by Pernak *et al.*[32]. Tang and Owen [4] calculated a critical $\chi_{crit} \approx 6.7$ for an ideal closed cavity with the dimensions of the experimental rig used here for validation.

Case 5 features strong effects of compressibility and χ of 5.34, approaching this critical value. Figure 18 shows the radial

Journal of Engineering for Gas Turbines and Power. Received September 14, 2023;
Accepted manuscript posted October 04, 2023. doi:10.1115/1.4063632

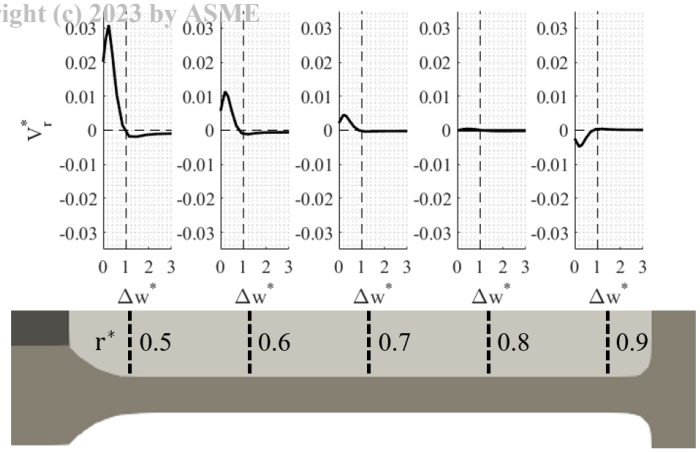

FIGURE 16: VARIATION OF RADIAL VELOCITY WITH WALL DISTANCE AT DIFFERENT RADIAL LOCATIONS FOR CASE 2

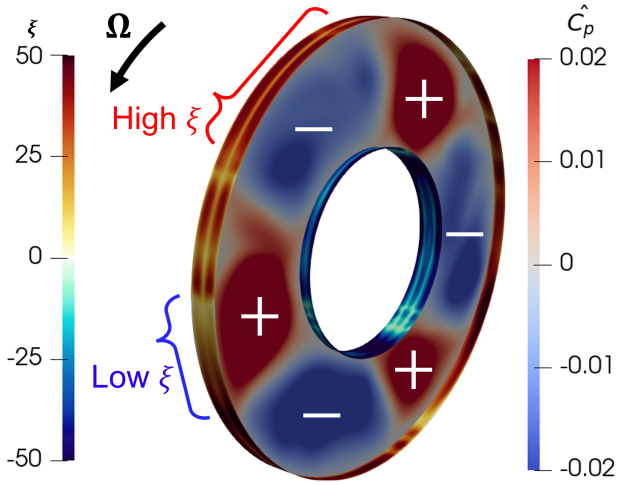

FIGURE 17: INSTANTANEOUS VARIATION OF HEAT FLUX ξ ON THE SHROUD AND HUB FROM CASE 2, JUXTA-POSED WITH NORMALISED PRESSURE PROFILE $\hat{C_p}$ IN THE CORE

distribution of disc temperature for Case 5 against Cases 2 and 4 from Figure 9. Also shown is the solution for pure conduction in a circular cylinder, given below:

$$\theta_d = \frac{ln(r/r_a)}{ln(r_b/r_a)}(\theta_{d,b} - \theta_{d,a}) + \theta_{d,a} \qquad (25)$$

where subscripts a and b respectively represent the inner and outer radii of the uniform disc diaphragm. The calculations show a consistent trend towards the pure conduction solution as χ approaches this critical value, deviating from the distribution seen in Cases 1-4.

This result is consistent with Figure 15 where the calculated plume mass flow rate shows a strong deviation from the trend of the experimental data. Again, the experiments are only valid for cases where the circumferential variation in pressure from the Rayleigh-Bénard convective vortices was strong enough to be measured.

The weakened buoyant structures have an effect on the shroud

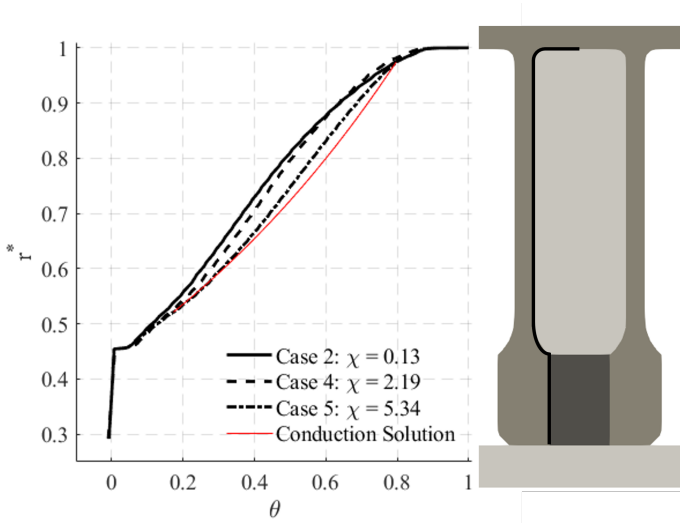

FIGURE 18: VARIATION OF DISC TEMPERATURE WITH RADIUS

heat transfer, as seen in Figure 11 with the high-χ outside the trend of the data. Without the formation of the cold anti-cyclonic vortices, the enhanced shroud heat transfer seen in buoyancy-induced flow does not occur.

4. CONCLUSIONS

This paper presents a complete study of conjugate heat transfer in compressor cavities that predicts the distribution of disc metal temperatures, rather than using such temperatures as a boundary condition. An original coupling strategy for the conjugate problem has been introduced, where unsteady Reynolds Averaged Navier-Stokes (URANS) simulations for the fluid are combined with a series of steady simulations for the solid domain. Application in this context is new, with existing conjugate approaches being steady-steady or unsteady-steady in the frequency domain. Success has been demonstrated through agreement with experiment in terms of the dynamics of the asynchronous rotating structures in the core, radial distributions of disc temperatures, radial mass flow rate within the buoyant core, and heat transfer correlations.

The computations provide important information not available to the experiments or theoretical models. The full distributions of temperatures in the metal (some not axisymmetric) are of practical importance to engine designers who aim to determine the radial growth of the discs and clearance of compressor blades. Further insight was provided in terms of the fluid mechanics of the laminar Ekman layers on the rotating discs. At low radius, the Ekman layers flow radially outward, with a reversal observed at high radius. This was linked to the balance of momentum in the cavity. The average speed of the core and structures were shown to be different. While the speed of the structures was invariant with radius there was radial asymmetry in the speed of the core, attributed to the interaction with lower momentum hot plumes and higher momentum cold plumes. The conjugate model captured the instantaneous circumferential variation of shroud heat transfer: the influence of the unsteady buoyant structures was identified with local regions of high and low heat transfer adja-

cent to cold and hot fluid vortices respectively.

The results have demonstrated how compressibility at large Reynolds numbers can lead to stratification. Under such circumstances the computed shroud heat transfer and corresponding buoyant structures were shown to be weak, and the radial distribution of disc temperature approached a profile expected from pure conduction. In terms of practical impact, the successful conjugate methodology provides accurate and expedient predictions vital to thermo-mechanical design tools for future engine architectures.

NOMENCLATURE

Roman letters

c_p	specific heat capacity [J/kgK]
D	width of bore annulus [m]
F_S	GCI safety factor
g	gravitational acceleration [m/s^2]
g_r	grid refinement ratio
h	heat transfer coefficient [W/m^{2}K]
H	specific enthalpy [m^2/s^2]
I	identity tensor
k	thermal conductivity [W/mK]
K	specific kinetic energy
$\dot{m}$	mass flow rate [kg/s]
n	number of vortex pairs
p	static pressure [Pa]
$\bar{p}$	mean static pressure
q	heat flux (W/m^2)
$\mathbf{q}$	heat flux vector
r	radius [m]
r^*	non-dimensional radius
s	hub width [m]
t	time [s]
T	temperature [K]
$\vec{\mathbf{V}}$	velocity flux
w	cavity width [m]
x	hub width [m]
x^*	non-dimensional hub width
y^+	non-dimensional wall distance

Greek letters

β	volumetric expansion coefficient [K^{-1}]
δ	thickness [m]
Δp	pressure gradient [Pa]
Δw	distance from cavity wall [m]
ε	relative error
θ	non-dimensional temperature
μ	dynamic viscosity [kg/ms]
ν	kinematic viscosity [m^2/s]
ξ	non-dimensional wall heat flux
ρ	density [kg/m^3]
τ	viscous stress tensor
Ω	angular velocity [rad/s]

Non-Dimensional Parameters

Bi	Biot number
C_p	pressure coefficient
$\hat{C_p}$	normalised pressure coefficient
C_w	flow coefficient
Gr	Grashof number
Ma	Mach number
Nu	Nusselt number
Pr	Prandtl number
Ra	Rayleigh number
Re_ϕ	rotational Reynolds number
$\beta\Delta T$	Buoyancy parameter
χ	compressibility parameter

Subscripts

a	value at base of disc diaphragm
adj	relative to the adjacent cavities
amb	value in ambient conditions
b	value at top of disc diaphragm
c	value in the fluid core
$crit$	critical value
cyl	value for free-cylindrical heat transfer condition
d	value of disc solid
Ek	value for Ekman layer
f	relative to the fluid
h	relative to hub
i	at the domain interface
s	relative to shroud
so	relative to disc outer shroud
r	radial direction
ro	for Rohacell
rel	evaluated in the relative reference of frame
T	relative to thermal boundary layer

ACKNOWLEDGEMENTS

Siemens-Energy funded the computational aspects of this research. The experimental work was funded by the UK Engineering and Physical Sciences Research Council (EPSRC), under grant number EP/P003702/1. This work used the Isambard UK National Tier-2 HPC Service operated by GW4 and the UK Met Office, and funded by EPSRC (EP/P020224/1) and the Cirrus UK National Tier-2 HPC Service at EPCC funded by the University of Edinburgh and EPSRC (EP/P020267/1).
The authors would like to thank Hrovje Jasak, Stefano Oliani and Roberto Maffuli for the constructive discussion and feedback.

DATA AVAILABILITY

Due to confidentiality agreements with research collaborators, supporting data can only be made available to bona fide researchers subject to a nondisclosure agreement. Details of how to request access are available at the University of Bath data archive.

REFERENCES

[1] Jackson, Richard W., Tang, Hui, Scobie, James A., Pountney, Oliver J., Sangan, Carl M., Owen, J. Michael and Lock, Gary D. "Analysis of Shroud and Disk Heat Transfer in Aero-Engine Compressor Rotors." *Journal of Engineering for Gas Turbines and Power* Vol. 143 No. 9 (2021): p. 091005.

[2] Owen, J. M. and Long, C. A. "Review of Buoyancy-Induced Flow in Rotating Cavities." *ASME. J. Turbomach.* Vol. 137 No. 11 (2015): p. 111001.

[3] Tritton, D. J. *Physical Fluid Dynamics*. Springer Science & Business Media.

[4] Tang, H. and Owen, J. M. "Plume Model for Buoyancy-Induced Flow and Heat Transfer in Closed Rotating Cavities." *ASME. J. Turbomach.* Vol. 145 No. 1 (2023): p. 011005.

[5] Tang, H. and Owen, J. M. "Theoretical Model of Buoyancy-induced Heat Transfer in Closed Compressor Rotors." *ASME. J. Eng. Gas Turbines Power* Vol. 140 No. 3 (2018): p. 032605.

[6] Owen, J. M., Tang, H. and Lock, G. D. "Buoyancy-Induced Heat Transfer inside Compressor Rotors: Overview of Theoretical Models." *Aerospace* Vol. 5 No. 1 (2018): p. 32.

[7] Pitz, D. B., Chew, J. W. and Marxen, O. "Large-Eddy Simulation of Buoyancy-Induced Flow in a Sealed Rotating Cavity." *ASME. J. Eng. Gas Turbines Power* Vol. 141 No. 2 (2019): p. 021020.

[8] Pitz, D. B. and Wolf, W. R. "Coriolis force effects on radial convection in a cylindrical annulus." *Int. J. Heat Mass Transfer* Vol. 189 (2022): p. 122650.

[9] Saini, D. and Sandberg, R. D. "Simulations of compressibility effects in centrifugal buoyancy-induced flow in a closed rotating cavity." *Int. J. Heat Fluid Flow* Vol. 85 (2020): p. 108656.

[10] Bohn, D., Deuker, E., Emunds, R. and Gorzelitz, V. "Experimental and Theoretical Investigations of Heat Transfer in Closed Gas-Filled Rotating Annuli." *ASME. J. Turbomach.* Vol. 117 No. 1 (1995): p. 175–183.

[11] Puttock-Brown, M. R., Rose, M. G. and Long, C. A. "Experimental and Computational Investigation of Rayleigh-Bénard Flow in the Rotating Cavities of a Core Compressor." *Proceedings of the ASME Turbo Expo 2017: Power for Land, Sea, and Air*, Vol. Volume 5B: Heat Transfer. Charlotte, North Carolina, USA, June 26-30, 2017. V05BT15A032.

[12] Puttock-Brown, M. R. and Rose, M. G. "Formation and Evolution of Rayleigh-Bénard Streaks in Rotating Cavities." *Proceedings of the ASME Turbo Expo 2018: Power for Land, Sea, and Air*, Vol. Volume 5B: Heat Transfer. Oslo, Norway, June 11-15, 2018. V05BT15A016.

[13] Saini, D. and Sandberg, R. D. "Large-Eddy Simulations of High Rossby Number Flow in the High-Pressure Compressor Inter-Disk Cavity." *ASME. J. Turbomach.* Vol. 143 No. 11 (2021): p. 111002.

[14] Atkins, N. R. "Investigation of a Radial-Inflow Bleed as a Potential for Compressor Clearance Control." *Proceedings of the ASME Turbo Expo: Power for Land, Sea, and Air*, Vol. 3A: Heat Transfer. Texas, USA, June 3–7, 2013. V03AT15A020.

[15] Gao, F. and Chew, J. W. "Flow and Heat Transfer Mechanisms in a Rotating Compressor Cavity Under Centrifugal Buoyancy-Driven Convection." *ASME. J. Eng. Gas Turbines Power* Vol. 144 No. 5 (2022): p. 051010.

[16] Jackson, R. W., Luberti, D., Tang, H., Pountney, O. J., Scobie, J. A., Sangan, C. M., Owen, J. M. and Lock, G. D. "Measurement and Analysis of Buoyancy-Induced Heat Transfer in Aero-Engine Compressor Rotors." *ASME. J. Eng. Gas Turbines Power* Vol. 143 No. 6 (2021): p. 061004.

[17] Sun, Z., Amirante, D., Chew, J. W and Hills, N. J. "Coupled Aerothermal Modeling of a Rotating Cavity with Radial Inflow." *ASME. J. Eng. Gas Turbines Power* Vol. 138 No. 3 (2016): p. 032505.

[18] Amirante, D., Adami, P. and Hills, N. J. "A Multifidelity Aero-Thermal Design Approach for Secondary Air Systems." *ASME. J. Eng. Gas Turbines Power* Vol. 143 No. 3 (2021): p. 031012.

[19] Tian, S. and Zhu, Y. "Disk Heat Transfer Analysis in a Heated Rotating Cavity With an Axial Throughflow." *Proceedings of the ASME Turbo Expo 2012: Power for Land, Sea, and Air*, Vol. 4: Heat Transfer, Parts A and B: pp. 2191–2199. Copenhagen, Denmark, June 11-15, 2012.

[20] Bohn, D. E., Deutsch, G.N., Simon, B. and Burkhardt, C. "Flow Visualisation in a Rotating Cavity With Axial Throughflow." *Proceedings of the ASME Turbo Expo 2000: Power for Land, Sea, and Air*, Vol. 3: Heat Transfer; Electric Power; Industrial and Cogeneration. Munich, Germany, May 8–11, 2000. V003T01A084.

[21] He, L. "Efficient Computational Model for Nonaxisymmetric Flow and Heat Transfer in Rotating Cavity." *ASME. J. Turbomach.* Vol. 133 No. 2 (2010): p. 021018.

[22] He, L. "Closely Coupled Fluid-Solid Interface Method with Moving-Average for LES Based Conjugate Heat Transfer solution." *Int. J. Heat Fluid Flow* Vol. 79 (2019): p. 108440.

[23] Hickling, T. and He, L. "LES-CHT for a Rotating Cavity With Axial Throughflow." *ASME. J. Turbomach.* Vol. 145 No. 6 (2022): p. 061006.

[24] Abbassi, M., Lahaye, D. and Vuik, K. "Modelling Turbulent Combustion Coupled with Conjugate Heat Transfer in OpenFOAM." *Numerical Mathematics and Advanced Applications ENUMATH 2019*. Springer (2021): pp. 1137–1145.

[25] Gao, F., Pitz, D. B. and Chew, J. W. "Numerical investigation of buoyancy-induced flow in a sealed rapidly rotating disc cavity." *International Journal of Heat and Mass Transfer* Vol. 147 (2020): p. 118860.

[26] Menter, F. R., Kuntz, M. and Langtry, R. "Ten years of industrial experience with the SST turbulence model." *Turbulence, heat and mass transfer* Vol. 4 No. 1 (2003): pp. 625–632.

[27] Nicholas, T., Scobie, J. A., Lock, G. D. and Tang, H. "Transient Heat Transfer and Temperatures in Closed Compressor Rotors." *Appl. Therm. Eng., submitted (2023)* (2023).

[28] Luberti, D., Patinios, M., Jackson, R. W., Tang, H., Pountney, O. J., Scobie, J. A., Sangan, C. M., Owen, J. M. and Lock, G. D. "Design and Testing of a Rig to Investigate Buoyancy-Induced Heat Transfer in Aero-Engine Compressor Rotors." *ASME. J. Turbomach.* Vol. 143 No. 4 (2021): p. 041030.

[29] Owen, J. M. and Rogers, R. H. *Flow and Heat Transfer in Rotating Disc Systems, Vol. 1: Rotor-Stator Systems*. Research Studies Press, Taunton, John Wiley, New York (1988).

[30] Roache, P. J. *Verification and Validation in Computational Science and Engineering*. Vol. 895. Hermosa Publishing, Albuquerque, New Mexico (1998).

[31] Lock, G. D., Jackson, R. W., Pernak, M., Pountney, O. J., Sangan, C. M., Owen, J. M., Tang, H. and Scobie, J. A. "Stratified and Buoyancy-Induced Flow in Closed Compressor Rotors." *ASME. J. Turbomach.* Vol. 145 No. 1 (2023): p. 011008.

[32] Pernak, M. J., Nicholas, T, Williams, J. T., Jackson, R. W., Tang, H., Lock, G. D. and Scobie, J. A. "Experimental Investigation of Transient Flow Phenomena in Rotating Compressor Cavities." *Proceedings of the ASME Turbo Expo 2023: Power for Land, Sea, and Air*. GT2023 - 102294. Boston, USA, June 26-30, 2023.

[33] Gao, F. and Chew, J. W. "Ekman Layer Scrubbing and Shroud Heat Transfer in Centrifugal Buoyancy-Driven Convection." *ASME J. Eng. Gas Turbines Power* Vol. 143 No. 7 (2021): p. 071010.